nature nanotechnology

Article

https://doi.org/10.1038/s41565-025-02079-9

Nanoscopic strain evolution in single-crystal battery positive electrodes

Received: 17 October 2024

Accepted: 23 October 2025

Published online: 16 December 2025

Check for updates

Jing Wang[1,2], Tongchao Liu[1] ✉, Weiyuan Huang[1], Lei Yu[3], Haozhe Zhang[1,2], Tao Zhou[3], Tianyi Li[4], Xiaojing Huang[5], Xianghui Xiao[5], Lu Ma[5], Martin V. Holt[3], Kun Ryu[2], Rachid Amine[6], Wenqian Xu[4], Luxi Li[4], Jianguo Wen[3], Ying Shirley Meng[2,7] ✉ & Khalil Amine[1,2] ✉

Single-crystal Ni-rich layered oxides (SC-NMC) with a grain-boundary-free configuration have effectively addressed the long-standing cracking issue of conventional polycrystalline Ni-rich materials (PC-NMC) in lithium-ion batteries, prompting a shift in optimization strategies. However, continued reliance on anisotropic lattice volume change—a well-established failure indicator in PC-NMC—as a metric for understanding strain and guiding compositional design for SC-NMC becomes controversial. Here, by leveraging multiscale diagnostic techniques, we unravelled the distinct nanoscopic strain evolution in SC-NMC during battery operation, challenging the conventional composition-driven strategies and mechanical degradation indicators used for PC-NMC. Through particle-level chemomechanical analysis, we reveal a decoupling between mechanical stability and lattice volume change in SC-NMC, identifying that structural instability in SC materials is primarily driven by multidimensional lattice distortions induced by kinetics-driven reaction heterogeneity and progressively deactivating chemical phases. Using this mechanical failure mode, we redefine the roles of cobalt and manganese in maintaining mechanical stability. Unlike cobalt's detrimental role in PC-NMC, we find cobalt to be critical in enhancing the longevity of SC-NMC by mitigating localized strain along the extended diffusion pathway, whereas manganese exacerbates mechanical degradation.

Nickel-rich $LiNi_xMn_yCo_zO_2$ ($x+y+z=1, x \geq 0.6$, Ni-rich nickel manganese cobalt oxide (NMC)) layered oxide positive electrode materials with a high accessible specific capacity (>200 mAh g^{-1}) are widely used in high-energy lithium-ion batteries (LIBs)[1–4]. However, mechanical degradation, primarily driven by external stress or internal lattice strain, remains a major challenge[5–8]. This degradation often leads to particle fracture, followed by surface parasitic reactions and irreversible phase transformation[9,10]. In particular, most of the existing commercial Ni-rich NMC are secondary particles (5–15 μm) composed of primary nanograins (50–500 nm), interconnected by grain boundaries[11,12]. Polycrystalline Ni-rich materials (PC-NMC) are inherently susceptible to mechanical instability because of the anisotropic lattice parameter changes (that is, expansion along the *c* direction and contraction along the *a*/*b* direction) during Li ions moving in and out of the lattice[13]. The repeated volume expansion and contraction during battery cycling subject the randomly oriented nanograins to severe compressive or

[1]Chemical Sciences and Engineering Division, Argonne National Laboratory, Lemont, IL, USA. [2]Pritzker School of Molecular Engineering, University of Chicago, Chicago, IL, USA. [3]Center for Nanoscale Materials, Argonne National Laboratory, Lemont, IL, USA. [4]X-ray Science Division, Advanced Photon Sources, Argonne National Laboratory, Lemont, IL, USA. [5]National Synchrotron Light Source II, Brookhaven National Laboratory, Upton, NY, USA. [6]Material Science Division, Argonne National Laboratory, Lemont, IL, USA. [7]Argonne Collaborative Center for Energy Storage Science (ACCESS), Argonne National Laboratory, Lemont, IL, USA. ✉e-mail: liut@anl.gov; shirleymeng@uchicago.edu; amine@anl.gov

tensile strain through the interactions between closely packed particles. The strain can be further exacerbated by the large lattice parameter changes and crystallographic anisotropy within the nanograins[14,15]. This creates intergranular cracks, facilitating liquid electrolyte solution penetration into the newly exposed surface and triggering additional interfacial degradation[16–18]. Accordingly, the magnitude of volume change becomes a common indicator for accessing strain accumulation and mechanical stability of PC-NMC[8,16,19–24].

To mitigate the mechanical degradation issue, modulating lattice volume evolution by optimizing cobalt (Co) and manganese (Mn) content in PC-NMC has been widely explored, as composition changes could substantially alter the electrochemical properties. Typically, Co mitigates Li/Ni disorder but promotes particle cracking due to exacerbated volume change and high lattice oxygen activity at deep delithiation states[5,19,25,26]. Conversely, Mn constrains lattice parameter changes and improves interfacial stability with stable Mn(IV)–O bonds, which comes at the cost of a lower initial cell capacity[19,27,28]. Consequently, low Co and even Co-free NMCs are considered a feasible approach to enhance structural stability at less cost[29–31]. Although the grain boundaries still exist, they pose potential risks for particle pulverization and surface deterioration, especially at high cell potentials.

Single crystallization has emerged as a promising strategy to enhance the multiscale structural integrity of NMC particles by eliminating grain boundaries[32,33]. Single-crystal Ni-rich layered oxides (SC-NMC) have a continuous crystal lattice without internal grain boundaries, with crystallite sizes between 1 µm and 10 µm (refs. 32,34,35). The single-crystal (SC) architecture not only facilitates a higher tap density at the electrode level but also eliminates intergranular cracking by reducing stress between particles arising from the anisotropic volume change. However, the larger crystal size inherent to SC particles significantly magnifies the impact of internal lattice strain, primarily driven by heterogeneous Li^+ (de)insertion through the extended diffusion pathways within the layered structure[36–38]. Despite this, the current understanding and characterization of strain in SC-NMC are often based on models developed for PC-NMC, where volume change serves as a key indicator[39–42]. Nonetheless, the actual volume change–strain performance (VSP) relationship in single particles, free from the grain-to-grain interactions of polycrystalline (PC) particles, is largely underexplored. Consequently, composition-driven strain engineering strategies for SC Ni-rich NMC may not align with previous observations in PC systems. Yet, there has been limited investigation into the actual strain evolution in SC particles. This gap is further compounded by the absence of methodically integrated, multiscale diagnostics techniques, which are essential for capturing how strain develops, evolves and impacts the structural stability and electrochemical performance.

Here we systematically investigate the interplay between lattice volume changes, nanoscopic strain and electrochemical failure in SC Ni-rich NMC, using both PC and SC Co-free $LiNi_{0.9}Mn_{0.1}O_2$ (NM91) and Mn-free $LiNi_{0.9}Co_{0.1}O_2$ (NC91) as model systems. Through multiscale characterizations, we elucidate the distinct strain evolution in SC Ni-rich NMC, challenging the previously established VSP relationship for conventional NMC-based battery systems. We reveal that a large volume change is not the prerequisite for severe strain accumulation (or lattice distortion); rather, the root cause lies in kinetically driven reaction heterogeneity. The presence of strain further exacerbates localized chemical and mechanical degradation, leading to capacity decay over cycling. In particular, contrary to previous observations in PC-NMC, we demonstrate that Mn is more mechanically detrimental than Co in SC-NMC. This is attributed to more heterogeneous intraparticle reactions and greater lattice strain due to sluggish kinetics in Co-free positive electrodes. Conversely, Co proves essential in SC Ni-rich NMC for improving cell capacity and electrode structural stability, striking a promising balance between cost, performance and sustainability. By simultaneously probing the chemical and mechanical aspects at both nano- and micrometre scales, our work provides meaningful insights into compositional optimization pathways in SC Ni-rich NMC, guiding the rational development of high-performance battery positive electrode materials.

Strain fundamentals and model systems

Strain has emerged as a key indicator of internal stress accumulation and mechanical degradation[7,43,44]. However, the understanding of strain remains ambiguous and inconsistent across the published peer-reviewed literature. To establish a clear framework for this study, we first outline some fundamentals of strain.

Strain (ε) refers to the structural deformation of a material in response to stress (σ)[45]. In the specific context of Ni-rich NMC, strain primarily arises from chemomechanical forces (for example, O–Li–O bonding and electrostatic repulsion) induced by Li insertion and extraction during electrochemical testing (Supplementary Fig. 1). In this work, it is mathematically represented as

$$\varepsilon = \frac{d_{\text{measured}} - d_0}{d_0}, \quad (1)$$

where d_{measured} and d_0 are interplanar spacings of the locally measured states and unstrained states of the crystal, respectively. In this definition, strain reflects the local deviation of lattice parameters from their equilibrium lattice configuration[46,47]. When the accumulated strain exceeds the elastic limit, it can lead to irreversible mechanical degradation (for example, intragranular or intergranular cracking). A detailed discussion of the origin, impact and methodology of strain is provided in Supplementary Note 1.

To investigate the VSP relationships for strategic composition-driven strain regulation in insertion chemistry, we have designed two comparable compositions, namely, Co-free NM91 and Mn-free NC91, as our models, featuring boundary-rich or boundary-free configurations. In these compositions, the same Ni content ensures a comparable state of charge (SoC), whereas variations in the Mn/Co content allow for a controlled regulation of lattice dimension changes. The VSP relationships are examined for conventional PC Ni-rich systems and further explored for SC Ni-rich layered oxides.

The Ni-rich NMC materials were synthesized via a co-precipitation and solid-state calcination process, yielding PC particles (~6–7 µm) with similar surface areas (Supplementary Figs. 2 and 3) and SC particles (~3–5 µm) with coherent and grain-boundary-free crystal structure (Supplementary Figs. 4 and 5). Both PC and SC samples have comparable stoichiometry (Ni:Mn ≈ 9:1 or Ni:Co ≈ 9:1) (Supplementary Table 1), uniform elemental distribution (Supplementary Figs. 6 and 7) and a hexagonal α-$NaFeO_2$ ($R\bar{3}m$) structure without impurities (Supplementary Fig. 8). The Co-free samples exhibit higher Li/Ni disorder than Mn-free counterparts, probably due to stronger magnetic frustration from Ni^{2+}/Ni^{3+} and Mn^{4+} (Supplementary Tables 2–5)[48].

Strain evolution in PC Ni-rich layered oxides

To understand strain evolution in PC layered oxides during Li metal coin cell cycling, lattice parameter changes are monitored via in situ X-ray diffraction (XRD) measurements. Figure 1a,b shows the two-dimensional (2D) contour plots of PC-NC91 and PC-NM91 during the first Li metal coin cell cycle at 20 mA g^{-1}. Both samples show a similar SoC-dependent shift during delithiation and lithiation, indicating solid-solution reactions within the layered structure (Supplementary Figs. 9–12 and Supplementary Note 2).

Due to the secondary particle morphology of PC-NMC, mechanical interaction among densely packed primary grains can generate compressive/tensile stress during lattice expansion/contraction (Supplementary Note 3). Rietveld refinements (Supplementary Fig. 13) reveal that both materials show similar *a*-axis changes, consistent with comparable Ni oxidation (Supplementary Fig. 14), but PC-NC91 exhibits a larger *c*-axis contraction (6.0% versus 3.6%) and greater

https://doi.org/10.1038/s41565-025-02079-9

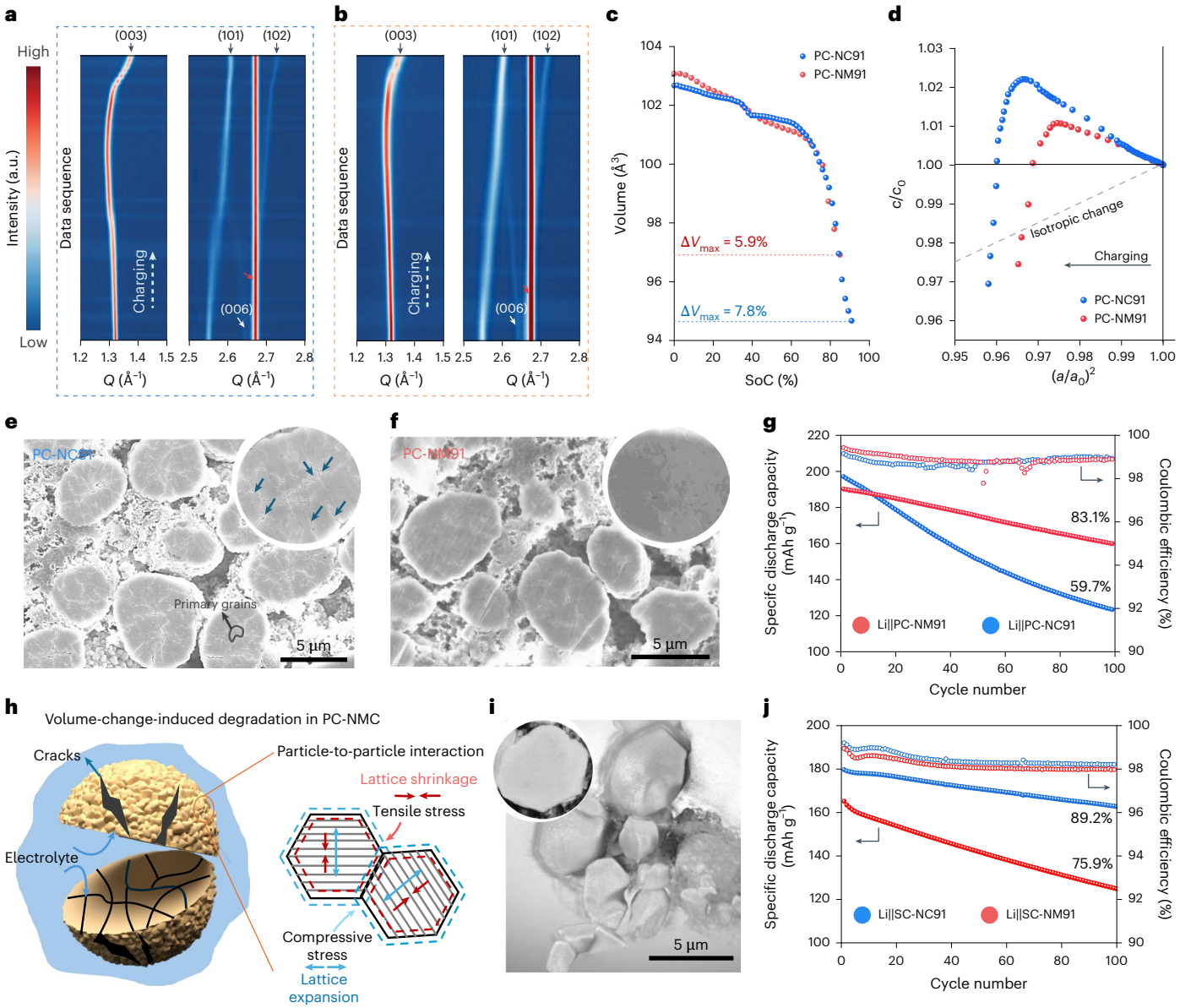

Fig. 1 | Structural, morphological and electrochemical characterizations of PC Ni-rich electrode active materials. a,**b**, 2D contour plots of in situ XRD for the phase evolution of PC-NC91 (**a**) and PC-NM91 (**b**) during the initial charge process in Li metal coin cell configuration at a specific current of 20 mA g^{-1}. The colour scale on the left represents the diffraction intensity of the shown peaks. The red arrows indicate the diffraction signals arising from the Al foil current collector of the positive electrode. **c**, Plot of lattice volume change during charging for both PC-NC91 and PC-NM91 at 20 mA g^{-1} in Li metal coin cell. **d**, Plot of c/c_0 versus $(a/a_0)^2$ for PC-NC91 and PC-NM91 charged at 20 mA g^{-1} in a Li metal coin cell configuration. The dotted grey line indicates the isotropic shrinkage of the crystal structure, whereas the solid grey line represents the condition $c/c_0 = 1$ (c_0 is the initial lattice parameter before cycling). **e**,**f**, FIB-SEM images of cycled PC-NC91 (**e**) and PC-NM91 (**f**) electrodes operated in the Li metal coin cell at 100 mA g^{-1} for 100 cycles. **g**, Galvanostatic cycling performance of Li||PC-NC91 and Li||PC-NM91 coin cells cycled at 100 mA g^{-1} (three formation cycles at 20 mA g^{-1} were conducted before the long-term cycling test). **h**, Schematic of the mechanical degradation mode in PC Ni-rich materials. **i**, 3D tomography image for SC-NC91, inserted with the FIB-SEM image showing the grain-boundary-free configuration. **j**, Cycling performance comparison for Li||SC-NC91 and Li||SC-NM91 coin cells cycled at 100 mA g^{-1} (three formation cycles at 20 mA g^{-1} were conducted before the long-term cycling test).

volume shrinkage (7.8% versus 5.9%; Fig. 1c), suggesting more stress accumulation at grain boundaries. Additionally, PC-NC91 deviates more strongly from isotropic dimensional change (Fig. 1d and Supplementary Fig. 15), suggesting faster mechanical stress build-up than PC-NM91. As shown in Supplementary Fig. 16, PC-NM91 and PC-NC91 exhibit similar Li diffusion rates throughout the charging process, suggesting the minimal impact of kinetic-induced reaction heterogeneity on stress formation.

Ex situ post-mortem focused-ion-beam (FIB) scanning electron microscopy (SEM) measurements are carried out to assess the impact of mechanical stress on the morphological evolution of positive electrodes. PC-NC91 exhibits apparent microcracks along the grain boundaries, which expand throughout the secondary particles (Fig. 1e). These observations suggest that tensile strain in PC-NC91 is released by grain separation inside particles, which facilitates liquid electrolyte solution infiltration and parasitic reactions within the particle interior. The PC-NM91, on the other hand, remains largely intact, exhibiting only minor vein-like features after 100 cycles (at 100 mA g^{-1}), indicating improved morphological stability (Fig. 1f). Consequently, the Li||PC-NM91 coin cell shows an improved cycling stability (83.1%),

attributed to the reduced grain separation and intergranular cracks (Fig. 1g) at the positive electrode. Conversely, the Li||PC-NC91 coin cell exhibits rapid degradation with a specific discharge capacity retention of 59.7% after 100 cycles (at 100 mA g^{-1}).

Anisotropic dimensional distortion and volume contraction, which are directly linked to strain within PC particles, promote particle fracture and grain boundary separation through strain relief, ultimately leading to the deterioration of layered oxides. This process defines the typical VSP relationships in PC-NMC positive electrodes (Fig. 1h).

Self-accelerated phase transition in SC Ni-rich layered oxides

Clearly, the established VSP relationships in PC-NMC are predominantly based on grain-to-grain interactions. However, in SC-NMC, where grain boundaries are absent (Fig. 1i and Supplementary Fig. 5), the role of volume change on structural evolution remains less understood. Interestingly, the Li||SC-NC91 coin cell demonstrates improved cycling stability (specific discharge capacity retention of 89.2% after 100 cycles at 100 mA g^{-1}) compared with the Li||SC-NM91 one (75.9%) for the same electrochemical testing conditions (Fig. 1j). These results contrast with prior studies of PC Ni-rich materials, thereby necessitating further investigation.

To track the lattice structure evolution in SC Ni-rich NMC, in situ XRD measurements were performed on Li||SC-NM91 and Li||SC-NC91 coin cells. The cells' potential profiles and corresponding dQ/dV curves are shown in Supplementary Fig. 17. As indicated in Fig. 2a and Supplementary Figs. 18 and 19, similar to the Li metal coin cells with PC positive electrodes, the Li metal coin cell testing of the SC-NC91 electrodes shows an SoC-dependent shift during charging, exhibiting solid-solution reactions. By contrast, substantial peak broadening of (003) is observed in Li metal coin cells with SC-NM91, which starts at 4.1 V and persists at the end of charging, suggesting the presence of multiple phases (Fig. 2b and Supplementary Figs. 20 and 21). In particular, no significant broadening of the (101) peak is observed at high SoCs, probably due to increased Ni valence and strengthened Ni–O bonding[49,50].

The four-point probe conductivity measurements, galvanostatic intermittent titration technique (GITT) and Li metal coin cell rate capability test measurements and analyses show that the intrinsic differences in Li-ion diffusion and reaction rate are influenced by the Mn/Co content. These features align well with previous reports regarding Ni-rich NMC materials[27] and suggest that the Co-containing SC-NC91 shows better kinetics than Co-free SC-NM91 (Supplementary Figs. 22–24 and Supplementary Notes 4 and 5) in Li metal coin cells. The impact from these intrinsic kinetic differences could be amplified by the long diffusion pathways in SC Ni-rich particles, especially at fast cycling rates of Li metal coin cells[38].

To understand the kinetic effects in phase evolution, the in situ XRD measurements of both positive electrode materials were carried out in a Li metal coin cell configuration at a specific current of 200 mA g^{-1} (Fig. 2c,d). In the Li||SC-NC91 coin cell, the accelerated charge–discharge rate obscures the H2–H3 phase transition at the positive electrode due to reduced delithiation (Fig. 2c and Supplementary Figs. 25 and 26). Yet, the (003) reflection maintains a single-phase evolution with a symmetrical shape until the end of charging. Interestingly, SC-NC91 shows a strong correlation between the peak position and delithiation states at different specific currents (Fig. 2h (left) and Supplementary Note 6). However, for SC-NM91, more pronounced peak broadening and separation emerge from 4.3 V, presenting the H2–H3 phase transition process (Fig. 2d and Supplementary Figs. 27 and 28). The fast reaction rate exacerbates lattice parameter changes and phase separation in SC-NM91, inducing partially deep delithiated phases inside particles (Supplementary Note 7 and Fig. 2h (right)). The degree of delithiation is closely linked to the Ni oxidation states, which can affect the structure of the transition metal (TM) layer (MO_2). In particular, the a-lattice parameter change after charge for the Li||SC-NM91 cell cycled at 200 mA g^{-1} is similar to the change at 20 mA g^{-1} rate (Supplementary Fig. 29), despite the different SoC achieved. This suggests that the partially deep delithiated phases may enhance TM–O orbital overlap and activate oxygen redox (Supplementary Note 8)[51], accelerating positive electrode structural degradation and capacity loss in Li||SC-NM91 cells. Consequently, the difference in discharge capacity retentions of Li||SC-NC91 and Li||SC-NM91 cells cycled at 200 mA g^{-1} (15%) becomes larger than that at 100 mA g^{-1}(13.3%) (Supplementary Fig. 30).

Williamson–Hall (W–H) analysis shows negligible crystallite size effects and peak broadening dominated by microstrain (Supplementary Fig. 31). The quantitative refinement results on a- and c-lattice parameters, volume change and microstrain are shown in Fig. 2e–g and Supplementary Figs. 32–34. The (003) reflections were then deconvoluted by assuming a single phase or the coexistence of two phases based on the refinement results (Fig. 2a–d and Supplementary Note 9). The sluggish Li-ion diffusion in SC-NM91 with a long diffusion length leads to the co-existence of the H2–H3 phase, distinguished by significant differences in lattice parameters (Δc_{max} = 0.68 Å). Observations of the phase transitions at various specific currents suggest a self-accelerating reaction within the SC-NM91 particle (Supplementary Note 10). The outer 'shell' reaches the H3 phase earlier, with a more contracted lattice, blocking Li-ion movement from the core and promoting strain accumulation. Therefore, though SC-NC91 and SC-NM91 exhibit comparable microstrain values at low SoCs, SC-NM91 exhibits a rapid increase in microstrain at higher cell potentials, as well as at faster cycling conditions (that is, 200 mA g^{-1}).

SC-NC91 exhibits a larger lattice parameter change and more pronounced anisotropic dimensional change compared with SC-NM91 (Supplementary Fig. 35), yet still delivers improved cycling performance in a Li metal coin cell. This contrasts with the behaviour of PC Ni-rich NMC, where electrochemical stability is closely correlated with lattice dimensional changes. Therefore, in Li metal coin cells with SC Ni-rich NMC positive electrode active materials, cycling stability appears to be predominantly governed by the degree of intraparticle crystallographic homogeneity, requiring spatial resolution techniques to correlate bulk-level phase separation with the lattice and chemical structure at the particle level.

Nanoscale mapping for crystal and chemical structures

Nanofocused scanning X-ray diffraction microscopy (SXDM) was performed to analyse the strain spatially within single particles. The principle of SXDM is illustrated in Fig. 3a and described in detail in Supplementary Note 11. The reasons for selecting the (003) Bragg reflection to investigate strain are further discussed in Supplementary Note 12. Figure 3b illustrates three types of observed lattice distortion from SXDM: strain (interlayered expansion/contraction $\Delta d/d$) and lattice rotation in the Q_x–Q_y plane (bending θ_{xy}) and the Q_x–Q_z plane (bending θ_{xz}). It should be noted that the observed strain or rotation indicated in Fig.3 is not related to the distortion of the MO_6 octahedral layers, but rather reflects changes in the relative orientation and d spacings of the average lattice in the crystalline lattice.

The results of ex situ SXDM mapping for the two positive electrode samples charged to 4.5 V and after 100 cycles at 100 mA g^{-1} in Li metal coin cell configuration are shown in Fig. 3c–f. The standard deviations of the $\Delta d/d$, θ_{xy} and θ_{xz} values show the degree of distortions over particles (Fig. 3g–i). The charged SC-NC91 particle exhibits a homogeneous lattice with a narrow d-spacing distribution and high crystalline quality, as reflected by the uniform diffraction intensity and a symmetric one-dimensional (1D) rocking curve (Supplementary Figs. 36 and 37). By contrast, the total diffraction intensity for the charged SC-NM91 is less detectable except for the centre (Supplementary Fig. 38). Additionally, the 1D rocking curve shows an asymmetric shape

https://doi.org/10.1038/s41565-025-02079-9

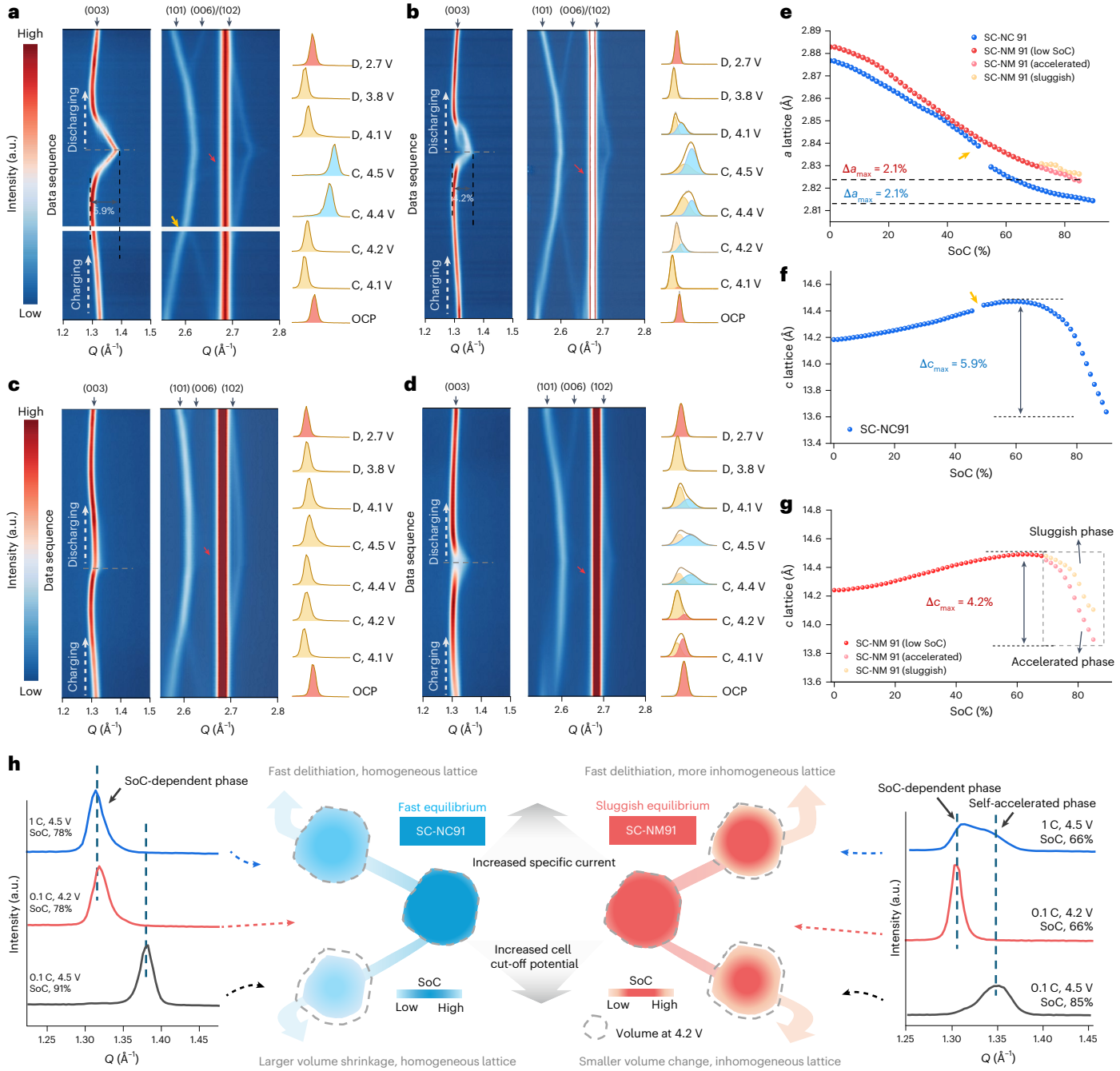

Fig. 2 | Phase evolutions of SC samples under different specific currents. **a**,**b**, 2D contour plots of in situ XRD for the structural evolution of SC-NC91 (**a**) and SC-NM91 (**b**) during the initial charge and discharge cycle in Li metal coin cell configuration at a specific current of 20 mA g^{-1}. The colour scale on the left represents the diffraction intensity of the shown peaks. **c**,**d**, 2D contour plots of in situ XRD for the structural evolution of SC-NC91 (**c**) and SC-NM91 (**d**) during the initial charge and discharge cycle in Li metal coin cell configuration at a specific current of 200 mA g^{-1}. The colour scale on the left represents the diffraction intensity of the shown peaks. Impurities marked by the red arrows arise from the Li metal negative electrode and Al foil current collector at the positive electrode. The selected (003) reflections at different potentials are shown on the right of each figure (red, yellow and blue refer to the deconvoluted H1, H2 and H3 phases, respectively). OCP denotes the open-circuit potential, and the prefixes C and D indicate the charged and discharged states, respectively. For all the selected (003) peaks, the *x* axis represents the scattering vector *Q* (1.27–1.42 Å^{-1}), and the *y* axis represents the diffraction intensity (a.u.). **e**–**g**, Results from Rietveld refinements for *a*-lattice parameter changes at 20 mA g^{-1} (**e**) and *c*-lattice parameter changes for SC-NC91 (**f**) and SC-NM91 (**g**) during the initial charge at 20 mA g^{-1} in the Li metal coin cell configuration. The terms accelerated (faster phase evolution) and sluggish (slower lattice response) describe the relative kinetics of lattice change during delithiation in SC-NM91. **h**, Schematic of the different phase evolutions of the two SC Ni-rich materials. The graphs show the correlation between peak position and delithiation states at different specific currents and cut-off potentials. SC-NC91 shows SoC-dependent (003) peak shift, whereas SC-NM91 shows exacerbated phase separation at a higher specific current and cut-off potential. The yellow arrow in **a**, **e** and **f** indicates the data gap caused by an unexpected beam interruption during the battery test.

https://doi.org/10.1038/s41565-025-02079-9

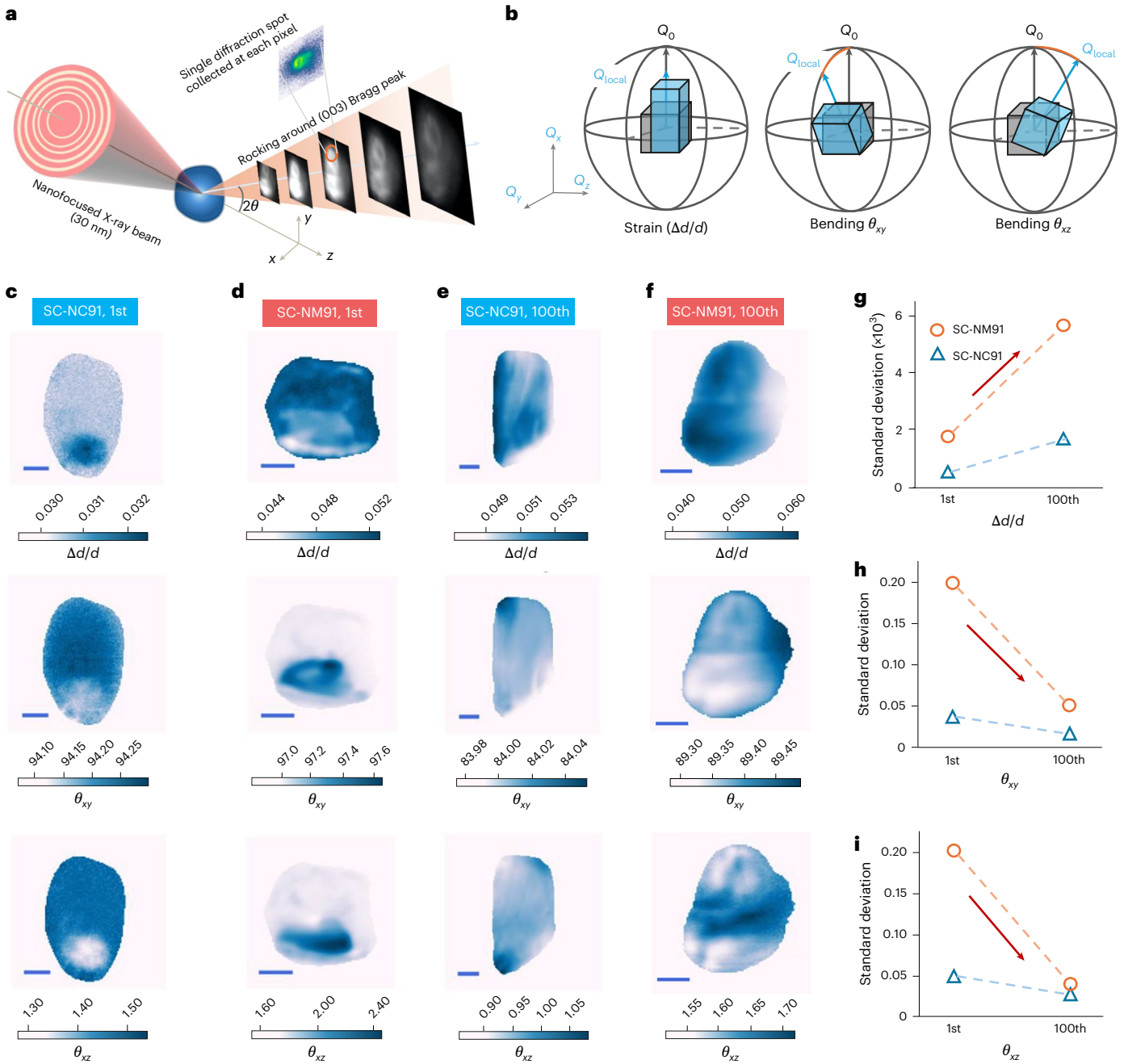

Fig. 3 | Localized lattice distortion profiles inside SC particles cycled at various electrochemical conditions. a, Schematic of SXDM used in this work. **b**, Schematic of two types of lattice distortion: lattice expansion/contraction ($\Delta d/d$) and lattice rotation (bending θ_{xy} and bending θ_{xz}). Here Q_{local} indicates the locally measured value, whereas Q_0 is the momentum transfer vector for the unstrained state. In all the cases presented here, Q_0 is chosen as the momentum transfer for the 003 reflection. **c**,**d**, $\Delta d/d$, θ_{xy} and θ_{xz} mapping for fully charged SC-NC91 (**c**) and SC-NM91 (**d**) after the first charge process in Li metal coin cells applying a specific current of 20 mA g^{-1} and cut-off potential of 4.5 V. **e**,**f**, $\Delta d/d$, θ_{xy} and θ_{xz} mapping for fully charged SC-NC91 (**e**) and SC-NM91 (**f**) after 100 cycles in Li metal coin cells applying a specific current of 100 mA g^{-1} and cut-off potential of 4.5 V. The colour scales for each map in **e** and **f** are individually adjusted based on the maximum and minimum values of the respective dataset. **g**–**i**, Quantitative comparison for strain (**g**), θ_{xy} (**h**) and θ_{xz} (**i**) of SC-NC91 and SC-NM91 at the 1st and 100th cycles. The *y* axis shows the calculated standard deviations (σ) of local $\Delta d/d$, θ_{xy} and θ_{xz} values over the particle. Scale bars, 1 µm (**c**–**f**).

with a larger peak width compared with SC-NC91 (Supplementary Fig. 39), aligning well with the (003) peak separation in the XRD. The SXDM mapping confirms that the charged SC-NM91 particle shows severe lattice distortion, with a larger interlayer spacing variation of 0.0018—more than three times larger than that of SC-NC91. Additionally, higher magnitudes of twisting and bending are observed in SC-NM91, suggesting larger crystal orientations or rotations generated during charging.

It is noticed that for both samples, the strain is increased whereas the lattice rotation is decreased after long-term battery testing (Fig. 3g–i). This may be attributed to the gradual release of misorientation distortion (that is, lattice rotation) caused by intragranular cracking and irreversible phase transitions to spinel and rock-salt (RS) phases. However, lattice strain can intensify due to the increased lattice mismatch between the newly formed phases and the remaining layered structures. In particular, Fig. 3c–f shows that $\Delta d/d$ mostly anticorrelates

with θ_{xy} and θ_{xz} spatially, further suggesting the competing evolution of strain and misorientation distortion. SC-NC91 retains low heterogeneity and misorientation, with distortions mainly near particle surfaces (Fig. 3e), probably from the commonly observed lattice mismatch at the positive electrode–liquid electrolyte interface[52]. However, lattice strain in SC-NM91 becomes more pronounced after cycling, with *d*-spacing heterogeneity 3.3 times larger than that of cycled SC-NC91, accompanied by a marked reduction in rotational distortions. This suggests a lattice-strain-dominated degradation over long-term cycling (Fig. 3f). Interestingly, although SC-NC91 exhibits a larger change in the *c*-lattice parameter during delithiation, it shows less distortion and greater structural stability, suggesting that strain is more closely linked to local lattice deviations from the expected state than to the absolute lattice changes during delithiation.

On the basis of the above observations, lattice strain is decoupled from the lattice parameter changes in SCs. However, the origins of this strain and its role in mechanical degradation require further investigation. Moreover, due to the smaller variation in the *a*-lattice parameter and weaker intensity of reflections such as (101), (102) and (104), the diffraction-based techniques are relatively difficult to access in-plane strain. However, X-ray absorption spectroscopy (XAS) is sensitive to local bond lengths and distortions around TMs[53,54], providing insight into strain development within MO_2 layers. Thus, XAS was further used to correlate phase evolution with chemical properties. Mn and Co ions mostly remain electrochemically inactive (Supplementary Fig. 40), not contributing additional cell capacity. Meanwhile, both SC-NM91 and SC-NC91 demonstrate a relatively reversible Ni K-edge shift and Ni–O bond length changes during the initial charge–discharge cycle (Supplementary Figs. 41 and 42 and Supplementary Tables 6 and 7). However, SC-NM91 shows a slightly more pronounced increase in local structural disorder after discharge, suggesting the correlation of Ni redox behaviour with structural reversibility. An in-depth investigation into the local chemical structure evolution at the particle level is required.

Full-field transmission X-ray microscopy (TXM) coupled with three-dimensional (3D) X-ray absorption near-edge structure (XANES) measurements was further conducted to analyse the chemical origins of strain. Figure 4a,b shows the Ni oxidation state distribution (manifested by colour variations) for charged SC-NC91 and SC-NM91 at 4.5 V, based on the white-line (WL) energy of Ni K edge. The cross-sectional chemical mappings from three different directions (that is, *x*–*y*, *y*–*z* and *x*–*z*) demonstrate a homogeneous Ni valence across the SC-NC91 particles (Fig. 4a). By contrast, a large portion of the charged SC-NM91 particles exhibit high oxidation states within the bulk (Fig. 4b). The histogram for statistical analysis of each 3D dataset shows that SC-NC91 has a higher average WL energy than SC-NM91, which is consistent with the XAS results (Supplementary Fig. 43). Despite this, SC-NM91 has a wider Ni oxidation state distribution, implying the coexistence of chemical phases with various lattice parameters, which contributes to the strain generation inside particles[55]. Moreover, the deep delithiated states (Supplementary Note 13) triggered by the inhomogeneous reaction inside the particles may contribute to irreversible lattice distortions arising from σ-type hybridization between Ni^{3+}/Ni^{4+} and the O^{2-} species[56]. Specifically, although the average SoC and Ni valence state of SC-NM91 is lower than SC-NC91 at the end of charge, the partial deeper delithiated regions may activate the charge compensation from oxygen, which may eventually exacerbate the integrity of the MO_2 layers. This observation is consistent with the sluggish change in the *a*-lattice parameters observed in XRD. Additionally, the broad distribution of Ni valence states corresponds well with phase separation in SC-NM91, and the pronounced *d*-spacing heterogeneity in SXDM strain mapping, together suggesting the co-evolution of in-plane strain.

Figure 4e,f shows the 3D TXM-XANES results of both samples after cycling in the Li metal coin cell configuration. Even though more lithium is extracted from SC-NC91 per cycle, the positive electrode active material still exhibits a uniform Ni oxidation state in particles. Nonetheless, more red regions are observed for SC-NM91 even in the discharged state, suggesting the existence of an inactive Ni-related phase and explaining the capacity loss of the Li||SC-NM91 coin cell over cycling. The formation of electrochemically fatigued phases in SC-NM91 may be linked to the release of misorientation distortion and escalation of localized lattice strain, as demonstrated in the SXDM analysis. The overall Ni valence in the cycled SC-NM91 particles appears increased due to the irreversible Li-ion extraction and insertion, as evidenced by the XANES data of the cycled positive electrodes (Fig. 4g and Supplementary Fig. 44). These observations are consistent with the contraction of the Ni–O bond length and larger increase in Debye–Waller disorder factor (σ^2_{Ni-O}) of cycled SC-NM91, indicating the presence of electrochemically fatigued phases and increased structural disorder after cycling (Supplementary Figs. 45 and 46 and Supplementary Tables 8 and 9)[57,58]. Further statistical analysis of the WL peak position shows a wider Ni valence distribution in SC-NM91 than in SC-NC91 (Fig. 4h). The chemical heterogeneity observed closely correlates with the strain accumulation observed in SXDM and XRD, suggesting the chemical origins of strain formation.

Atomic-scale observation of strain accumulation

The investigation into the impact of lattice strain and reaction heterogeneity on morphology and lattice structure was conducted using high-resolution transmission electron microscopy (TEM). The low-magnification observations (Fig. 5a,g) reveal that after prolonged cycling in the Li metal coin cell configuration, the surface structures of both types of positive electrode sample underwent a transformation into the RS phase. This transformation should be attributed to the surface parasitic reduction between Ni^{4+} reactions and the carbonate-based liquid electrolyte solution, which is commonly observed in Ni-rich layered oxides and appears to be independent of Mn and Co contents[19,59]. As shown by the electron diffraction patterns at the subsurface regions (Supplementary Fig. 47), pronounced lattice distortion is revealed in cycled SC-NM91 by the presence of streak-like diffraction features, which are typically associated with stacking faults and disrupted periodicity between adjacent MO_2 layers. As depicted in Fig. 5b–d and Supplementary Fig. 48, SC-NC91 maintains an intact structure without any observable microcracks after long-term cell cycling. Conversely, the cycled SC-NM91 exhibits notable morphological damage, evident intragranular cracks and the presence of an RS phase near the cracks (Fig. 5h–j and Supplementary Fig. 49). The transition from a layered (Li_xTMO_2) to an RS (NiO-like) structure is often associated with lattice oxygen loss, which manifests as a suppressed O K-edge pre-edge peak in electron energy-loss spectroscopy[60]. As shown in Supplementary Fig. 50, the O pre-edge peak intensity not only decreases near the surface of SC-NM91 but also exhibits a relatively low intensity across the cracks, aligning with the RS phase observed in Fig. 5h. These results imply that the extensive intragranular cracking formation in SC-NM91 is accompanied by lattice oxygen loss and TM migration, which are probably arising from the stronger TM–O orbital overlap at the partially deep delithiated regions in SC-NM91, as suggested by the in situ XRD and TXM-XANES results (Supplementary Note 14). Besides, the geometric phase analysis reveals substantial strain primarily concentrated around the cracking region of SC-NM91 (Fig. 5k,l), whereas SC-NC91 exhibits a more well-maintained lattice structure without apparent strain accumulation (Fig. 5e,f). The spatial co-location of microcracks and spinel/RS phases near the crack regions in SC-NM91 aligns with the opposing trends of strain and rotation observed in Fig. 3c–i, suggesting the coupled evolution of strain and lattice rotation as a key driver of mechanical failure and capacity decay (Supplementary Note 15 and Supplementary Figs. 52 and 53). The chemomechanical evolutions impacted by the Mn/Co content in SC structures are summarized in Fig. 5m, and further discussed in Supplementary Note 16.

https://doi.org/10.1038/s41565-025-02079-9

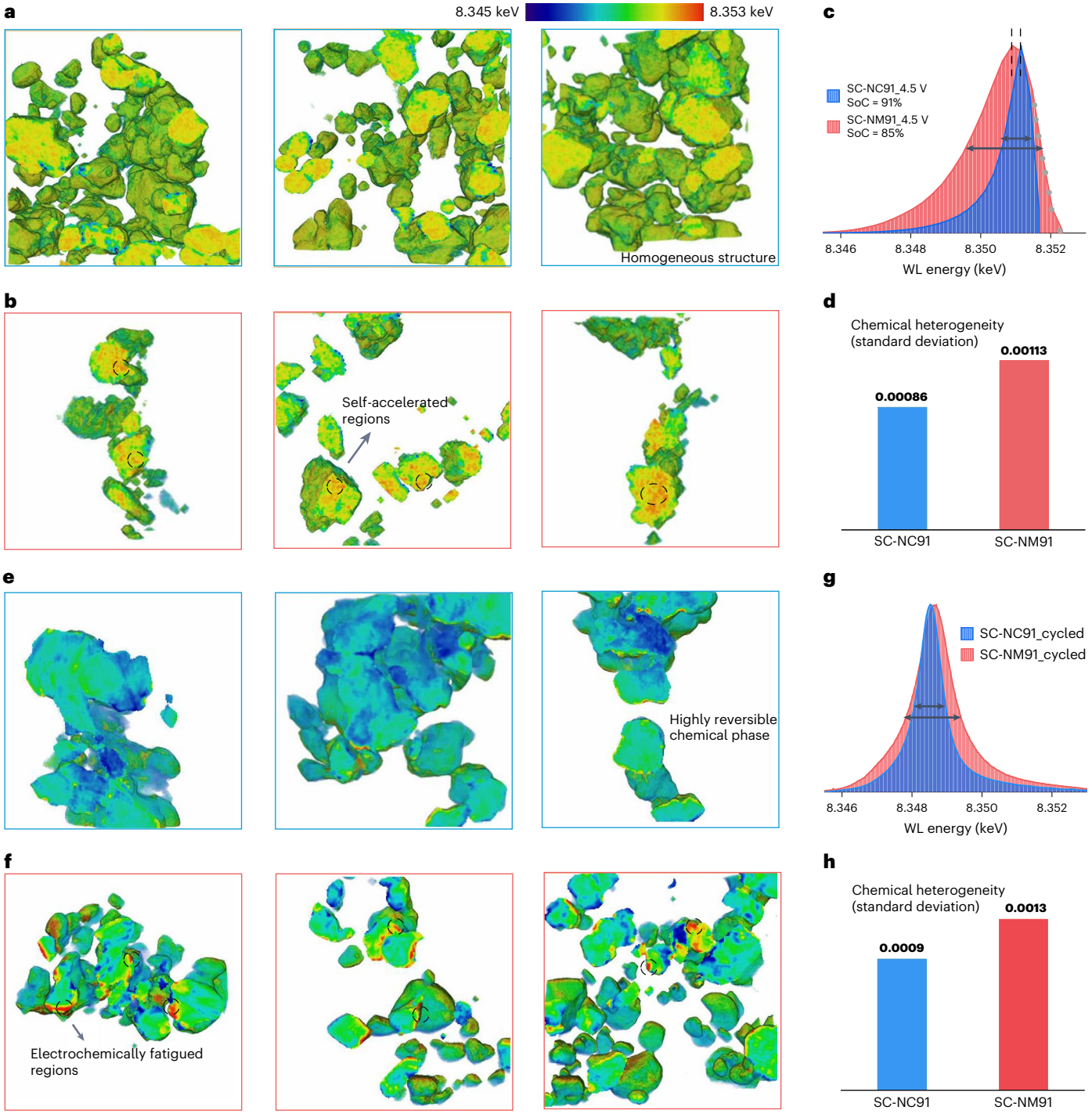

Fig. 4 | 3D chemical phase distribution of SC particles at charged state and after electrochemical cycling. a,**b**, 3D TXM-XANES mappings based on the Ni WL peak position for SC-NC91 (**a**) and SC-NM91 (**b**) particles at a charged Li metal cell potential of 4.5 V (specific current applied during cycling is 20 mA g^{-1}). From left to right: cross-sectional views of chemical mapping along the *x*–*y*, *y*–*z* and *x*–*z* planes. **c**, Corresponding WL peak position in statistics based on approximately 10^6 pixels for the above charged SC-NC91 and SC-NM91 particles. The black arrows indicate the relatively narrow and broad distributions of Ni oxidation states in the two samples. The grey dots show that the highly oxidized Ni-related phases are present in the above charged SC-NM91 particles. The errors for the statistical results are around 0.02 eV. **d**, Chemical heterogeneity shown by the calculated standard deviation of the WL peak position in the statistics based on **c**. **e**,**f**, 3D TXM-XANES mappings based on the WL peak position for cycled SC-NC91 (**e**) and cycled SC-NM91 (**f**) particles operated at a Li metal cell after 100 cycles in the cell potential range of 4.5 V (specific current applied during cycling of 100 mA g^{-1}). **g**, Corresponding WL peak position in statistics for the above cycled SC-NC91 and cycled SC-NM91 particles. **h**, Chemical heterogeneity shown by the calculated standard deviation of the WL peak position in statistics based on the data in **g**.

Conclusions

By integrating multiple diagnostic techniques, we have uncovered distinct nanoscopic strain evolution in SC Ni-rich battery positive electrode active materials, redefining the role of composition on the electrochemical cycling stability of Li||NMC coin cells. Differing from PC-NMC, the strain in SC-NMC is decoupled from the magnitude of lattice parameter changes. Instead, the reaction heterogeneity can lead to accelerated delithiation inside active material particles, resulting in

https://doi.org/10.1038/s41565-025-02079-9

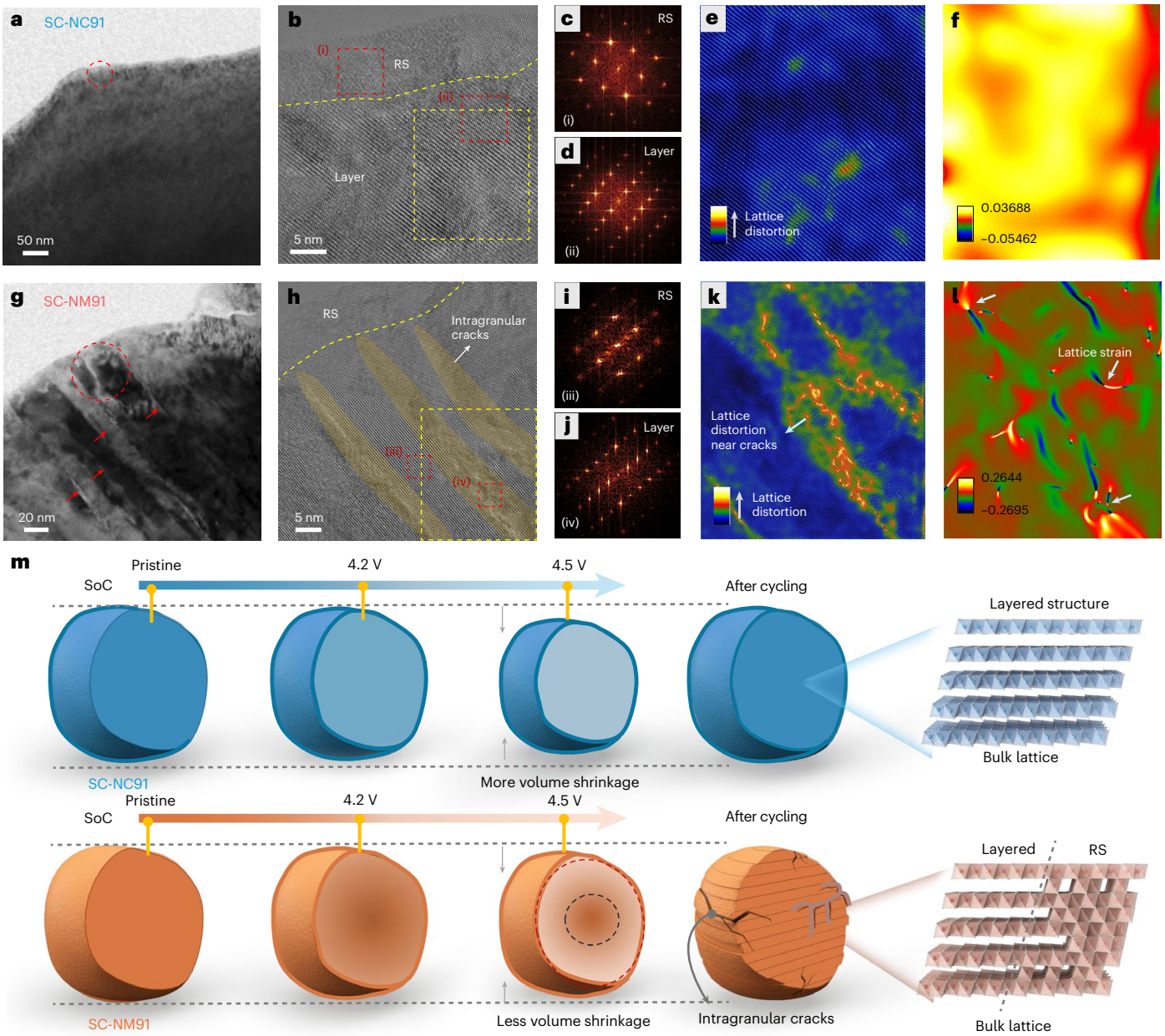

Fig. 5 | Atomic-scale analysis of localized structural and mechanical degradation of SC particles after electrochemical cycling. a,**g**, Low-magnification TEM image of cycled SC-NC91 (**a**) and cycled SC-NM91 (**g**) particles after 100 cycles in the Li metal coin cell configuration using a cell potential range of 2.7–4.4 V and a specific current of 100 mA g^{-1}. **b**,**h**, High-magnification TEM image of the above cycled SC-NC91 (**b**) and cycled SC-NM91 (**h**) particles. The selected regions are indicated by red circles in **a** and **g**. **c**,**d**, Selected-area diffraction images collected from positions indicated by the red boxes (i; **c**) and (ii; **d**) in **b**, corresponding to the rock-salt and layered domains, respectively. **i**,**j**, Selected-area diffraction images collected from positions indicated by the red boxes (iii; **i**) and (iv; **j**) in **h**, corresponding to the rock-salt and layered domains, respectively. **e**,**k**, Inverse fast Fourier transform image of the above cycled SC-NC91 (**e**) and cycled SC-NM91 (**k**) particles applying a mask (Supplementary Fig. 51). **f**,**l**, Strain fields of the above cycled SC-NC91 (**f**) and cycled SC-NM91 (**l**) observed by a geometric phase analysis. **m**, Schematic of the mechanism of chemomechanical evolutions for SC-NC91 and SC-NM91 during electrochemical cycling in Li metal coin cell configuration applying a cell potential in the range of 2.7–4.4 V and a specific current of 100 mA g^{-1}. The black circle indicates the kinetically hindered zones. The region between the red and black circles schematically shows the presence of a self-accelerating delithiation reaction.

localized regions of intensified strain generation, ultimately diminishing the battery performance. We observed that the compositional effects deviate from the observations in PC Ni-rich materials. Mn exacerbates reaction heterogeneity, which promotes oxygen loss and strain accumulation, whereas Co enables fast structural equilibrium and highly reversible structural changes during Li metal coin cell charge–discharge cycles. As a result, Co-containing SC positive electrodes, compared with their Co-free SC counterparts, enable higher coin cell discharge specific capacity, improved cycling stability and good rate capability. These results elucidate distinct strain modulation pathways compared with conventional NMC and redefine the roles of Mn and Co in mechanical stability in SC Ni-rich NMC. It is important to point out that although these fundamental insights are crucial for understanding the mechanical and structural changes in SC- and PC-NMC positive electrodes, demonstrating the practical application of this mechanistic knowledge at a high technology readiness level requires further optimization of the active material's composition and structure and focus on the engineering process of electrode production and cell preparation[61,62].

Online content

Any methods, additional references, Nature Portfolio reporting summaries, source data, extended data, supplementary information, acknowledgements, peer review information; details of author contributions and competing interests; and statements of data and code availability are available at https://doi.org/10.1038/s41565-025-02079-9.

References

1. Li, M., Lu, J., Chen, Z. & Amine, K. 30 years of lithium-ion batteries. *Adv. Mater.* **30**, 1800561 (2018).
2. Schmuch, R., Wagner, R., Hörpel, G., Placke, T. & Winter, M. Performance and cost of materials for lithium-based rechargeable automotive batteries. *Nat. Energy* **3**, 267–278 (2018).
3. Li, W., Erickson, E. M. & Manthiram, A. High-nickel layered oxide cathodes for lithium-based automotive batteries. *Nat. Energy* **5**, 26–34 (2020).
4. Goodenough, J. B. & Park, K. S. The Li-ion rechargeable battery: a perspective. *J. Am. Chem. Soc.* **135**, 1167–1176 (2013).
5. Liu, T. et al. Rational design of mechanically robust Ni-rich cathode materials via concentration gradient strategy. *Nat. Commun.* **12**, 6024 (2021).
6. Yan, P. et al. Intragranular cracking as a critical barrier for high-voltage usage of layer-structured cathode for lithium-ion batteries. *Nat. Commun.* **8**, 14101 (2017).
7. Bi, Y. et al. Reversible planar gliding and microcracking in a single-crystalline Ni-rich cathode. *Science* **370**, 1313–1317 (2020).
8. Zhang, R. et al. Compositionally complex doping for zero-strain zero-cobalt layered cathodes. *Nature* **610**, 67–73 (2022).
9. Lin, F. et al. Surface reconstruction and chemical evolution of stoichiometric layered cathode materials for lithium-ion batteries. *Nat. Commun.* **5**, 3529 (2014).
10. Lee, S., Su, L., Mesnier, A., Cui, Z. & Manthiram, A. Cracking vs. surface reactivity in high-nickel cathodes for lithium-ion batteries. *Joule* **7**, 2430–2444 (2023).
11. Yan, P. et al. Tailoring grain boundary structures and chemistry of Ni-rich layered cathodes for enhanced cycle stability of lithium-ion batteries. *Nat. Energy* **3**, 600–605 (2018).
12. Xu, G. L. et al. Challenges and strategies to advance high-energy nickel-rich layered lithium transition metal oxide cathodes for harsh operation. *Adv. Funct. Mater.* **30**, 2004748 (2020).
13. Zhou, Y. N. et al. Tuning charge-discharge induced unit cell breathing in layer-structured cathode materials for lithium-ion batteries. *Nat. Commun.* **5**, 5381 (2014).
14. Mukhopadhyay, A. & Sheldon, B. W. Deformation and stress in electrode materials for Li-ion batteries. *Prog. Mater. Sci.* **63**, 58–116 (2014).
15. Stallard, J. C. et al. Mechanical properties of cathode materials for lithium-ion batteries. *Joule* **6**, 984–1007 (2022).
16. Ryu, H.-H., Park, K.-J., Yoon, C. S. & Sun, Y.-K. Capacity fading of Ni-rich $Li[Ni_xCo_yMn_{1-x-y}]O_2$ ($0.6 \le x \le 0.95$) cathodes for high-energy-density lithium-ion batteries: bulk or surface degradation? *Chem. Mater.* **30**, 1155–1163 (2018).
17. Li, W., Asl, H. Y., Xie, Q. & Manthiram, A. Collapse of $LiNi_{(1-x-y)}Co_{(x)}Mn_{(y)}O_{(2)}$ lattice at deep charge irrespective of nickel content in lithium-ion batteries. *J. Am. Chem. Soc.* **141**, 5097–5101 (2019).
18. Xu, C. et al. Bulk fatigue induced by surface reconstruction in layered Ni-rich cathodes for Li-ion batteries. *Nat. Mater.* **20**, 84–92 (2021).
19. Liu, T. et al. Understanding Co roles towards developing Co-free Ni-rich cathodes for rechargeable batteries. *Nat. Energy* **6**, 277–286 (2021).
20. Zhao, X. & Ceder, G. Zero-strain cathode materials for Li-ion batteries. *Joule* **6**, 2683–2685 (2022).
21. Xu, G.-L. et al. Building ultraconformal protective layers on both secondary and primary particles of layered lithium transition metal oxide cathodes. *Nat. Energy* **4**, 484–494 (2019).
22. Zhang, W. et al. Ni-rich $LiNi_{0.8}Co_{0.1}Mn_{0.1}O_2$ coated with Li-ion conductive Li_3PO_4 as competitive cathodes for high-energy-density lithium ion batteries. *Electrochim. Acta* **340**, 135871 (2020).
23. Yu, H. et al. Surface enrichment and diffusion enabling gradient-doping and coating of Ni-rich cathode toward Li-ion batteries. *Nat. Commun.* **12**, 4564 (2021).
24. Goonetilleke, D. et al. Alleviating anisotropic volume variation at comparable Li utilization during cycling of Ni-rich, Co-free layered oxide cathode materials. *J. Phys. Chem. C* **126**, 16952–16964 (2022).
25. Li, H. et al. Is cobalt needed in Ni-rich positive electrode materials for lithium ion batteries?. *J. Electrochem. Soc.* **166**, A429–A439 (2019).
26. Olivetti, E. A., Ceder, G., Gaustad, G. G. & Fu, X. Lithium-ion battery supply chain considerations: analysis of potential bottlenecks in critical metals. *Joule* **1**, 229–243 (2017).
27. Aishova, A., Park, G. T., Yoon, C. S. & Sun, Y. K. Cobalt-free high-capacity Ni-rich layered $Li[Ni_{0.9}Mn_{0.1}]O_2$ cathode. *Adv. Energy Mater.* **10**, 1903179 (2019).
28. Sun, Y. K., Lee, D. J., Lee, Y. J., Chen, Z. & Myung, S. T. Cobalt-free nickel rich layered oxide cathodes for lithium-ion batteries. *ACS Appl. Mater. Interfaces* **5**, 11434–11440 (2013).
29. Park, G.-T. et al. Introducing high-valence elements into cobalt-free layered cathodes for practical lithium-ion batteries. *Nat. Energy* **7**, 946–954 (2022).
30. Li, W., Lee, S. & Manthiram, A. High-nickel NMA: a cobalt-free alternative to NMC and NCA cathodes for lithium-ion batteries. *Adv. Mater.* **32**, 2002718 (2020).
31. Mu, L. et al. Dopant distribution in Co-free high-energy layered cathode materials. *Chem. Mater.* **31**, 9769–9776 (2019).
32. Qian, G. et al. Single-crystal nickel-rich layered-oxide battery cathode materials: synthesis, electrochemistry, and intra-granular fracture. *Energy Storage Mater.* **27**, 140–149 (2020).
33. Langdon, J. & Manthiram, A. A perspective on single-crystal layered oxide cathodes for lithium-ion batteries. *Energy Storage Mater.* **37**, 143–160 (2021).
34. Shi, J.-L. et al. Size controllable single-crystalline Ni-rich cathodes for high-energy lithium-ion batteries. *Natl Sci. Rev.* **10**, nwac226 (2023).
35. Moiseev, I. A. et al. Single crystal Ni-rich NMC cathode materials for lithium-ion batteries with ultra-high volumetric energy density. *Energy Adv.* **1**, 677–681 (2022).
36. Ge, M. et al. Kinetic limitations in single-crystal high-nickel cathodes. *Angew. Chem. Int. Ed.* **60**, 17350–17355 (2021).
37. Zou, Y. G. et al. Mitigating the kinetic hindrance of single-crystalline Ni-rich cathode via surface gradient penetration of tantalum. *Angew. Chem. Int. Ed.* **60**, 26535–26539 (2021).
38. Pandurangi, S. S., Hall, D. S., Grey, C. P., Deshpande, V. S. & Fleck, N. A. Chemo-mechanical analysis of lithiation/delithiation of Ni-rich single crystals. *J. Electrochem. Soc.* **170**, 050531 (2023).
39. Liu, J. et al. Understanding the synthesis kinetics of single-crystal Co-free Ni-rich cathodes. *Angew. Chem. Int. Ed.* **62**, e202302547 (2023).
40. Fan, X. et al. In situ inorganic conductive network formation in high-voltage single-crystal Ni-rich cathodes. *Nat. Commun.* **12**, 5320 (2021).
41. Sun, J. et al. The origin of high-voltage stability in single-crystal layered Ni-rich cathode materials. *Angew. Chem. Int. Ed.* **61**, e202207225 (2022).
42. Kim, K.-E. et al. Enhancing high-voltage structural stability of single-crystalline Ni-rich $LiNi_{0.9}Mn_{0.05}Co_{0.05}O_2$ cathode material by ultrathin Li-rich oxide layer for lithium-ion batteries. *J. Power Sources* **601**, 234300 (2024).

43. Liu, T. et al. Origin of structural degradation in Li-rich layered oxide cathode. *Nature* **606**, 305–312 (2022).
44. Heenan, T. M. et al. Identifying the origins of microstructural defects such as cracking within Ni-rich NMC811 cathode particles for lithium-ion batteries. *Adv. Energy Mater.* **10**, 2002655 (2020).
45. Yang, B. *Stress, Strain, and Structural Dynamics: An Interactive Handbook of Formulas, Solutions, and MATLAB Toolboxes* (Academic Press, 2005).
46. Chen, C. et al. Highly crystalline multimetallic nanoframes with three-dimensional electrocatalytic surfaces. *Science* **343**, 1339–1343 (2014).
47. Liu, D. et al. Strain analysis and engineering in halide perovskite photovoltaics. *Nat. Mater.* **20**, 1337–1346 (2021).
48. Zheng, J. et al. Ni/Li disordering in layered transition metal oxide: electrochemical impact, origin, and control. *Acc. Chem. Res.* **52**, 2201–2209 (2019).
49. Liu, S. et al. Origin of phase separation in Ni-rich layered oxide cathode materials during electrochemical cycling. *Chem. Mater.* **35**, 8857–8871 (2023).
50. Jousseaume, T., Colin, J.-F., Chandesris, M., Lyonnard, S. & Tardif, S. Strain and collapse during lithiation of layered transition metal oxides: a unified picture. *Energy Environ. Sci.* **17**, 2753–2764 (2024).
51. Ogley, M. J. et al. Metal–ligand redox in layered oxide cathodes for Li-ion batteries. *Joule* **9**, 101775 (2025).
52. Li, H., Zhang, N., Li, J. & Dahn, J. R. Updating the structure and electrochemistry of Li_xNiO_2 for $0 \le x \le 1$. *J. Electrochem. Soc.* **165**, A2985–A2993 (2018).
53. Olszewski, W. et al. The role of the local structural properties in the electrochemical characteristics of $Na_{1-x}Fe_{1-y}Ni_yO_2$ cathodes. *Mater. Today Energy* **40**, 101519 (2024).
54. Mao, Y. et al. High-voltage charging-induced strain, heterogeneity, and micro-cracks in secondary particles of a nickel-rich layered cathode material. *Adv. Funct. Mater.* **29**, 1900247 (2019).
55. Ryu, H.-H. et al. Capacity fading mechanisms in Ni-rich single-crystal NCM cathodes. *ACS Energy Lett.* **6**, 2726–2734 (2021).
56. Yu, H. et al. Restraining the escape of lattice oxygen enables superior cyclic performance towards high-voltage Ni-rich cathodes. *Natl Sci. Rev.* **10**, nwac166 (2023).
57. Balasubramanian, M., Sun, X., Yang, X. & McBreen, J. In situ X-ray diffraction and X-ray absorption studies of high-rate lithium-ion batteries. *J. Power Sources* **92**, 1–8 (2001).
58. Usoltsev, O. et al. Operando multi-edge XAS to reveal the effect of Co in Li-and Mn-rich NMC Li-ion cathodes. *Mater. Today Energy* **50**, 101853 (2025).
59. Sun, H.-H. & Manthiram, A. Impact of microcrack generation and surface degradation on a nickel-rich layered $Li[Ni_{0.9}Co_{0.05}Mn_{0.05}]O_2$ cathode for lithium-ion batteries. *Chem. Mater.* **29**, 8486–8493 (2017).
60. Qian, D., Xu, B., Chi, M. & Meng, Y. S. Uncovering the roles of oxygen vacancies in cation migration in lithium excess layered oxides. *Phys. Chem. Chem. Phys.* **16**, 14665–14668 (2014).
61. Frith, J. T., Lacey, M. J. & Ulissi, U. A non-academic perspective on the future of lithium-based batteries. *Nat. Commun.* **14**, 420 (2023).
62. Scurtu, R.-G. et al. From small batteries to big claims. *Nat. Nanotechnol.* **20**, 970–976 (2025).

Methods

Materials synthesis

$Ni_{0.9}Mn_{0.1}(OH)_2$ and $Ni_{0.9}Co_{0.1}(OH)_2$ precursors were prepared by a co-precipitation method in a 4-l batch reactor. Stoichiometric quantities of $NiSO_4{\cdot}6H_2O$ (Sigma-Aldrich, ≥98%) with either $MnSO_4{\cdot}H_2O$ (Sigma-Aldrich, ≥99%) or $CoSO_4{\cdot}7H_2O$ (Sigma-Aldrich, ≥99%) were dissolved in deionized water to form 2-M solutions. The TM sulfate solutions were pumped into the reactor, along with 4 M of NaOH and 6 M of $NH_3{\cdot}H_2O$, which served as chelating agents. The reactions occurred under a nitrogen atmosphere, with the pH maintained at 11.5, stirring at 1,000 rpm and the temperature controlled at 60 °C. Afterwards, the precursor powders were washed (three times with Millipore ultrapure water, about 18.2 MΩ cm), filtered under a vacuum (using a Büchner funnel equipped with Whatman Grade 41 quantitative filter paper and a side-arm flask) and vacuum dried at 80 °C overnight. The precursors were then thoroughly mixed with $LiOH{\cdot}H_2O$ as the lithium source (Li:TM = 1.03:1) using a Resodyn Acoustic Mixer (PharmaRAM I, Resodyn Acoustic Mixers) operated at a medium-level intensity for 3 min per cycle under ambient air at room temperature (25 °C) to ensure homogeneous blending. PC-NM91 was synthesized by sintering $Ni_{0.9}Mn_{0.1}(OH)_2$ at 740 °C for 12 h at a heating rate of 2 °C min^{-1} in a tubular furnace (Lindberg/Blue M, Thermo Scientific) under an O_2 atmosphere. PC-NC91 was synthesized by sintering $Ni_{0.9}Co_{0.1}(OH)_2$ at 720 °C for 12 h at the same heating rate and atmosphere. SC-NM91 was synthesized by sintering $Ni_{0.9}Mn_{0.1}(OH)_2$ at 900 °C for 2 h, followed by 870 °C for 10 h in the tubular furnace (Lindberg/Blue M, Thermo Scientific) at a heating rate of 4 °C min^{-1} under an O_2 atmosphere. Similarly, SC-NC91 was obtained by sintering $Ni_{0.9}Co_{0.1}(OH)_2$ at 880 °C for 2 h and 850 °C for 10 h in the tubular furnace under identical conditions with SC-NM91. Finally, the powders were carefully ground using an agate mortar and pestle inside an argon-filled glovebox (O_2 < 10 ppm, H_2O < 0.5 ppm) at room temperature (~25 °C) for about 10 min to obtain fine powders. The resulting materials were stored in a nitrogen-filled container at room temperature (~25 °C) before electrode fabrication.

Electrode preparation and electrochemical measurements

The positive electrodes were prepared by mixing the active materials with carbon black (C45 Conductive Carbon Black, TIMCAL, purity of >99.9%, average particle size of ~110 nm, Brunauer–Emmett–Teller surface area of 45 $m^2 g^{-1}$, average porosity of ~0.4 $cm^3 g^{-1}$ and average pore diameter of ~35 nm) and polyvinylidene fluoride (Solvay 5130) binder dissolved in *N*-methyl-2-pyrrolidone (Sigma-Aldrich; anhydrous, 99.5% purity, water content of <0.005%) in an 8:1:1 mass ratio. The mixture was then homogenized using a planetary centrifugal mixer (THINKY MIXER ARE-310) with highly polished yttria-stabilized zirconia grinding balls at 2,000 rpm for 8 min under ambient air in the wet-mixing mode. The resulting slurry was cast onto aluminium (Al) foil current collectors (MTI Corporation, purity of >99.3%, 15 ± 1 µm thick) using a tape-casting coater with a vacuum chuck (MSK-AFA-III, MTI Corporation) equipped with a film applicator set to an initial wet-coating thickness of 180 µm. The Al foil was used as received without additional surface cleaning or pretreatment. The coated electrodes were dried at 75 °C for 2 h, followed by calendering (roll pressing) to achieve a uniform thickness and improved electrode density (a final electrode porosity in the range of 20%–30%, calculated from the electrode thickness, mass loading and theoretical densities of individual components). The electrodes were passed through the rollers (Durston DRM C100 RE 100-mm combination rolling mill) multiple times at a gap setting of ~50 µm under an estimated pressure of 50–70 MPa to ensure consistent densification. The calendared sheets were then punched into circular electrodes (14-mm diameter) using a NOGAMI handheld electrode punch inside an argon-filled glovebox (O_2 < 10 ppm, H_2O < 0.5 ppm) at room temperature (25 ± 2 °C) to prevent moisture exposure. Subsequently, the electrodes were transferred to a vacuum oven (Thermo Fisher Precision Vacuum Oven, Model 29) and dried overnight at 60 °C to remove the residual solvent. The final mass loading of the active material in the positive electrode was approximately 4 mg cm^{-2}. The final electrodes were circular discs with a diameter of 14 mm (1.54 cm^2) and a dry thickness of ~35 µm.

The 2032-type coin cells (Canrd Technology Co. Ltd.) were assembled in an argon-filled glovebox (NEXUS-II VAC-ATM, O_2 < 10 ppm, H_2O < 0.5 ppm, room temperature) using stainless steel casing components, including a cathode cap, anode cap, two stainless steel spacers and a wave spring. Li metal foil (15-mm diameter, 200-µm thickness, purity 99.9%; Alfa Aesar) was used as the negative electrode, Celgard 2325 (25 µm thick, 39% porosity, average pore size of ~0.06 µm, 16-mm diameter) was used as separators and 1.2 M of $LiPF_6$ in EC/EMC (3:7) was used as the electrolyte (40 µl). The electrolyte was purchased as a preprepared solution (SelectiLyte BASF, battery grade, water content of <20 ppm). The electrolyte was stored in its original Al-laminated pouch at room temperature in an argon-filled glovebox and used directly without further purification. During cell assembly, the electrolyte was handled exclusively inside the glovebox using disposable polypropylene pipette tips and an Eppendorf Research Plus mechanical pipette to prevent contamination.

The cells were sealed using a coin cell crimping machine (Hohsen Automatic Coin Cell Crimper) with factory-calibrated pressure control. Galvanostatic charge–discharge cycling was performed using a NEWARE battery testing system (CT-4008Tn-5V10mA-164, Shenzhen, China, 5 V/10 mA channels, accuracy of ±0.02% in full scale) inside a climatic chamber (Thermo Fisher Scientific Heratherm Advanced Protocol Microbiological Incubators, convection heating) maintained at 25 °C. Three formation cycles at 20 mA g^{-1} were conducted before the long-term cycling test at 100 mA g^{-1}. All electrochemical measurements were performed using two different coin cells per condition, and the data presented represent the average values from both cells. The specific current and specific capacity reported in this study are calculated based on the mass of active materials in the positive electrode.

GITT measurements were carried out using a Maccor electrochemical analyser at a constant specific current of 20 mA g^{-1} in the potential range of 2.8–4.5 V. Each titration consisted of a 20-min current pulse followed by 140-min open-circuit relaxation to allow the system to reach near-equilibrium. Potential was recorded every second (that is, 1 s) throughout the pulse period. To determine the lithium-ion diffusion coefficient D_{Li}, we used the following equation:

$$D = \frac{4}{9\pi}\left(\frac{r_p}{\tau}\frac{\Delta E_s}{dE/d\sqrt{t}}\right)^2, \quad (2)$$

where r_p is the effective lithium-ion diffusion length, approximated by the average particle radius in SEM (ImageJ analysis of average particle diameter), τ is the duration of the current pulse, ΔE_s is the change in equilibrium potential during the rest period, E is the electrode potential, t is the step time and $dE/d\sqrt{t}$ is the initial slope of potential versus t (excluding the transition region), determined consistently in $10 < \sqrt{t} < 20$ for all samples. The analysis approach is consistent with prior GITT studies[63,64]. Demonstrations of the linearity of E_{pulse} versus $\sqrt{t}$ plots during GITT measurement and the methods used to extract $dE/d\sqrt{t}$ and ΔE_s are illustrated in Supplementary Figs. 54–56.

For thin-film electronic conductivity measurements, a standard four-point probe configuration was used, with a constant current applied between the outer probes and the potential drop was measured across the inner probes. The sheet resistivity was calculated using the following equation:

$$\rho = \frac{\pi t}{\ln[2]} \times \frac{V}{I}, \quad (3)$$

where t is the film thickness and V and I are the measured potential and applied current, respectively. The corresponding electronic

conductivity was obtained as $\sigma = \frac{1}{\rho}$. For the powder samples pressed into pellets, the electronic resistivity was determined using $\rho = \frac{wt}{L} \times \frac{V}{I}$, where w, t and L are the pellet width, thickness and distance between potential probes, respectively. The measurements were evaluated at 25 °C, stepping the potential to 4.0 V with a target current of 100 µA.

Physicochemical characterization

High-energy XRD (HEXRD) data were collected at the 11-ID beamline (0.1665 Å) and the 17-BM beamline (0.4520 Å) of the Advanced Photon Source at Argonne National Laboratory using a PerkinElmer large-area detector. The powder samples were loaded into Kapton tubes and sealed in an argon-filled glovebox (NEXUS-II, VAC-ATM, O_2 < 10 ppm, H_2O < 0.5 ppm, room temperature) to prevent air exposure during XRD measurements. The powders were gently packed to ensure uniform density along the beam path, and the capillaries were sealed to prevent environmental contamination during measurement.

The raw 2D diffraction images collected from the area detectors were integrated into 1D patterns using GSAS-II software. The integration process involved importing the image files (for example, TIFF), calibrating the detector geometry using a standard (for example, CeO_2 or LaB_6), and adjusting the start/end azimuth and 2θ range to exclude beamstop shadows and detector edges. After calibration, the images were azimuthally integrated over the full or selected χ range to produce intensity versus 2θ profiles. The resulting 1D patterns were exported as text files for further structural or phase analysis via Rietveld refinements in GSAS-II. The instrument parameters are extracted by fitting the standard samples (for example, CeO_2 or LaB_6). For the powder XRD data, the following parameters were refined: lattice parameters (a, c) of the $R\bar{3}m$ unit cell, microstrain broadening (modelled as isotropic), Li/Ni cation disorder (refining the site occupancies on the 3a and 3b Wyckoff positions with the fixed Mn/Co content based on inductively coupled plasma optical emission spectroscopy results) and isotropic atomic displacement parameters (Uiso) for each atomic species (Supplementary Note 17). The peak profile was modelled using a pseudo-Voigt function (Gaussian–Lorentzian convolution), and the background was modelled using a Chebyshev-1 polynomial function with six coefficients.

XAS experiments were conducted at the 7-BM-B beamline of the National Synchrotron Light Source II (NSLS-II) at Brookhaven National Laboratory. The cycled electrodes were harvested from coin cells disassembled in an argon-filled glovebox (NEXUS-II, VAC-ATM, O_2 < 10 ppm, H_2O < 0.5 ppm, ultrahigh-purity argon gas (99.999%), room temperature). Cell disassembly was performed using a coin cell disassembler (Hohsen), and the electrodes were handled with plastic-tipped tweezers (Ideal-Tek). The harvested electrodes were transferred into glass vials and rinsed three times with 5 ml of anhydrous dimethoxyethane (Sigma-Aldrich, ≥99.5%, water content of <50 ppm) to remove the residual electrolyte. The rinsed electrodes were then dried under a dynamic vacuum (~10^{-2} mbar) for 15 min at room temperature using the vacuum antechamber of the glovebox. Both pristine and cycled electrodes were sealed with Kapton tape inside the glovebox to prevent air exposure during XAS measurements. The prepared sealed samples were then placed in vacuum bags before being taken out of the glovebox for ex situ measurement. All the XAS spectra were collected at ~25 °C with the transmission signals. XANES and EXAFS spectra were extracted and normalized following standard procedures in ATHENA[65,66]. EXAFS fitting was carried out in ARTEMIS over a k range of 3–12.8 Å^{-1} and a radial distance range of 1.2–3.0 Å, covering both first and second coordination shells. Structural parameters, including bond distance (R) and Debye–Waller factor (σ^2), were refined with the fixed coordination number (N = 6). The E_0 value was 8,350 eV, and the amplitude reduction factor (S_0^2) was set to 0.8 for Ni in a similar manner as previous reports[66,67]. The error bar estimation method was explained elsewhere[68].

SEM and energy-dispersive X-ray spectroscopy mapping were performed using a Hitachi S4700 at Center for Nanoscale Materials of Argonne National Laboratory. Cross-sectional samples were prepared with a ZEISS NVision 40 FIB-SEM. TEM, selected-area electron diffraction, energy-dispersive X-ray spectroscopy, electron energy-loss spectroscopy and high-resolution TEM were conducted using the Argonne chromatic aberration-corrected TEM device (FEI Titan 80-300ST with an image aberration corrector to compensate for both spherical and chromatic aberrations) at an accelerating voltage of 200 kV. TEM and high-resolution TEM measurements were conducted on cycled positive electrodes. After electrochemical cycling, the electrodes were harvested, rinsed and dried following the same procedure described above for the XAS sample preparation. The harvested electrodes were cut into rectangular pieces (approximately 5 × 5 mm^2) using stainless steel scissors (Ideal-Tek). Samples were mounted on a sample stage, sealed in an Ar-filled container and briefly exposed to air (almost a few seconds) during instrument loading. Thin-section TEM specimens were prepared using a ZEISS NVision 40 FIB-SEM dual-beam system with standard FIB lift-out procedures. The lamellae were initially thinned to ~200 nm using a 30-kV Ga-ion beam, followed by final polishing at 5 kV to remove surface damage before TEM observation. The geometric phase analysis was also conducted by using DigitalMicrograph software (Supplementary Note 18 provides details of the calculation process).

Elemental analysis of PC and SC NM91 and NC91 powders was conducted using inductively coupled plasma optical emission spectroscopy on an Agilent 5110 Synchronous Vertical Dual View instrument at the Center for Nanoscale Materials of Argonne National Laboratory. The powder samples were digested in a mixture in a 1:3 volume ratio of nitric acid (70%, Sigma-Aldrich) and hydrochloric acid (37%, Sigma-Aldrich) using a total acid volume of 10 ml per sample. The resulting solutions were then diluted to achieve Ni, Mn and Co concentrations in the range of 1–10 ppm for accurate quantification.

The specific surface areas of the PC-NM91 and PC-NC91 powders were measured using nitrogen adsorption–desorption isotherms obtained using a Micromeritics ASAP 2020 instrument. Before measurement, the samples were degassed under a vacuum at 120 °C for 12 h to remove the surface-adsorbed species. The surface area was calculated using the Brunauer–Emmett–Teller method based on the adsorption data in the relative pressure (P/P_0) range of 0.05–0.30.

In situ HEXRD

In situ HEXRD measurements were carried out at the 11-ID-C (for cell galvanostatic cycling at 200 mA g^{-1}) and 17-BM-B (for cell galvanostatic cycling at 20 mA g^{-1}) beamline at the Advanced Photon Source using a monochromatic X-ray beam with a beam size of approximately 500 µm × 500 µm. Electrochemical measurements for in situ XRD were conducted using modified 2032-type coin cells (same specifications as those described in the 'Electrode preparation and electrochemical measurements' section). The modified cell cases were supplied by Canrd Technology Co. Ltd., and feature circular windows (~5-mm diameter) punched into the stainless steel casing and spacer to allow X-ray transmission. The holes in the cases were sealed with Kapton tape to prevent air exposure and liquid electrolyte solution leakage. The electrolyte volume used in these modified cells was maintained at 40 µl. Galvanostatic charge–discharge cycling measurements were conducted using a MACCOR battery testing system during X-ray acquisition at different current densities within the cell potential range of 2.7–4.5 V. A certified CeO_2 standard (SRM 674b) was used to calibrate the instrumental parameters for diffraction analysis.

W–H analysis was conducted to deconvolute the contributions of crystallite size and microstrain to peak broadening[69]. The W–H analysis was conducted using multiple diffraction peaks within the relevant 2θ range, based on the following equation:

$$\frac{\beta_{hkl} \times \cos\theta}{K\lambda} = \frac{1}{D} + \frac{4 \times \varepsilon \sin\theta}{K\lambda}, \quad (4)$$

where β_{hkl} is the full-width at half-maximum of the Lorentzian-fitted peaks, θ is the Bragg angle, K is the Scherrer constant of 0.9, λ is the X-ray wavelength, D is the mean crystallite size and ε represents the microstrain.

Rietveld refinements were performed using the sequential refinement function in the GSAS-II software package to extract the lattice parameters and microstrain evolution of the in situ XRD datasets[70]. Given the negligible size effect based on the W–H analysis, the crystallite size was fixed based on SEM measurements. The two-phase refinements were conducted in the high-SoC regions when applicable. An example of the two-phase refinement in this work is provided in Supplementary Fig. 57.

Scanning diffraction X-ray microscopy

Scanning diffraction X-ray microscopy (SDXM) was conducted at the Hard X-ray Nanoprobe beamline (3-ID) at NSLS-II. For the SXDM measurement, the cycled electrodes were harvested from disassembled coin cells (see the sample preparation for the XAS experiment in the 'Physicochemical characterization' section) and prepared in a similar way as the XAS measurement. In particular, the SC particles were mechanically detached from the cycled electrode foil by gentle scraping using a plastic spatula (VWR International) inside an argon-filled glovebox (O_2 < 10 ppm, H_2O < 0.5 ppm, 25 ± 2 °C). Approximately 1–2 mg of the collected particles were transferred to a 10- m silicon substrate. The sample was stored and transported in an inert atmosphere to prevent air exposure before SXDM measurements. During the experiments, X-rays were focused to an ~30-nm spot size to illuminate the sample, with the crystal orientation adjusted to excite Bragg diffraction. A pixel-array detector was positioned to capture the diffracted patterns at each scan point, enabling spatially resolved diffraction measurements. The sample was rocked over a 2° range around the selected Bragg peak, whereas a 2D raster scan with a 50-nm step size was performed at each rocking angle. A five-dimensional dataset with each pixel of the 2D image related to a 3D rocking curve was produced. The final image resolution was determined by the convolution of the beam profile with the pixel size (50 × 50 nm^2). SXDM typically produces a 2D projected image of the 3D particle. The projection is along the direction of the incident beam. For the SXDM results shown in Fig. 3, the normal direction is along the incident-beam direction.

For SDXM analysis, we used the five-dimensional analysis widget of the Diffraction User Data Explorer software (the 'Code availability' section includes a link to the software). The concept of the five-dimensional analysis is described elsewhere[71]. The first step is to image-register the SDXM maps taken at different sample angles. From there, a 3D reciprocal space is generated for each pixel in the real-space map. A 3D Gaussian fitting or centre-of-mass calculation is performed to calculate the position of the Bragg peak in reciprocal space. The length of the Q vector is used to calculate the d spacing (equation (3) of ref. 71), whereas the angular deviation of the Q vector from its expected value is used to calculate the lattice rotation (equation (4) of ref. 71).

Full-field TXM imaging and 3D tomography

TXM imaging was conducted at 18-ID FXI beamline of NSLS-II of Brookhaven National Laboratory for generating the 3D nano-XANES datasets. The cycled electrodes were prepared in a similar way to the SXDM measurement. In this case, approximately 1–2 mg of the active material from the cycled electrode (for the cycled electrode harvesting and coin cell disassembly, see the sample preparation for the XAS experiment in the 'Physicochemical characterization' section) was dispersed directly onto Kapton tape by gentle scraping using a plastic spatula (VWR International) inside an argon-filled glovebox (O_2 < 10 ppm, H_2O < 0.5 ppm, 25 ± 2 °C). The particles sealed in Kapton tapes were then stored in vacuum bags and mounted onto the holder before TXM measurement. For the experiment at the 18-ID (FXI) beamline, we used a double-crystal Si(111) monochromator with a bandpass of $\Delta E/E \approx 10^{-4}$, corresponding to an energy resolution of better than 1 eV at ~8,350 eV. The TXM-XANES data were collected at energies between 8,340 and 8,360 eV. The step size used in the energy-dependent measurement was 1 eV. Subelectronvolt precision of the WL shift was obtained in this work through per-voxel fitting of the XANES spectra (Supplementary Fig. 58). The procedure of the fitting is described elsewhere[72,73].

The average intensity per pixel in the raw TXM data was about 10^4 photons, corresponding to an intensity uncertainty of 1% from shot noise variations. Intensity uncertainty from the read-out noise is negligible. For each energy point across the XANES spectrum, 3D tomographic reconstructions were obtained from a series of projection images captured as the sample is rotated from 0° to 180°. These projections were collected at fine angular intervals to ensure accurate reconstruction of the internal structure. The resulting voxel resolution of the tomographic reconstructions was 40 nm, allowing for a detailed visualization of nanoscale chemical and structural variations within the sample. TXM datasets were reconstructed using the scientific package TXM_Sandbox (https://github.com/xianghuix/TXM_Sandbox). The segmentation, quantification and visualization of the TXM results were performed with Dragonfly v.2022.2 (Comet Technologies; https://www.theobjects.com/dragonfly). Examples of XANES spectra extracted from 3D TXM-XANES data are shown in Supplementary Fig. 59.

Data availability

All data are available in the article or its Supplementary Information, which are also available from the corresponding authors upon request.

Code availability

The code used to analyse the SDXM data is available at https://hub.docker.com/r/danielzt12/dude.

References

63. Chien, Y.-C. et al. Rapid determination of solid-state diffusion coefficients in Li-based batteries via intermittent current interruption method. *Nat. Commun.* **14**, 2289 (2023).
64. Schied, T. et al. Determining the diffusion coefficient of lithium insertion cathodes from GITT measurements: theoretical analysis for low temperatures. *ChemPhysChem* **22**, 885–893 (2021).
65. Ravel, B. & Newville, M. ATHENA, ARTEMIS, HEPHAESTUS: data analysis for X-ray absorption spectroscopy using IFEFFIT. *J. Synchrotron Rad.* **12**, 537–541 (2005).
66. Tallman, K. R. et al. Nickel-rich nickel manganese cobalt (NMC622) cathode lithiation mechanism and extended cycling effects using operando X-ray absorption spectroscopy. *J. Phys. Chem. C* **125**, 58–73 (2020).
67. Chen, C.-H. et al. Operando X-ray diffraction and X-ray absorption studies of the structural transformation upon cycling excess Li layered oxide $Li[Li_{1/18}Co_{1/6}Ni_{1/3}Mn_{4/9}]O_2$ in Li ion batteries. *J. Mater. Chem. A* **3**, 8613–8626 (2015).
68. Newville, M. Fundamentals of XAFS. *Rev. Mineral. Geochem.* **78**, 33–74 (2014).
69. Williamson, G. & Hall, W. X-ray line broadening from filed aluminium and wolfram. *Acta Met.* **1**, 22–31 (1953).
70. Toby, B. H. & Von Dreele, R. B. GSAS-II: the genesis of a modern open-source all purpose crystallography software package. *J. Appl. Crystallogr.* **46**, 544–549 (2013).
71. Chahine, G. A. et al. Imaging of strain and lattice orientation by quick scanning X-ray microscopy combined with three-dimensional reciprocal space mapping. *J. Appl. Crystallogr.* **47**, 762–769 (2014).

72. Xiao, X., Xu, Z., Lin, F. & Lee, W.-K. TXM-Sandbox: an open-source software for transmission X-ray microscopy data analysis. *J. Synchrotron Radiat.* **29**, 266–275 (2022).
73. Xiao, X., Xu, Z., Hou, D., Yang, Z. & Lin, F. Rigid registration algorithm based on the minimization of the total variation of the difference map. *J. Synchrotron Radiat.* **29**, 1085–1094 (2022).

Acknowledgements

We acknowledge support from the US Department of Energy (DOE), Office of Energy Efficiency and Renewable Energy, Vehicle Technologies Office. Argonne National Laboratory is operated for DOE Office of Science by UChicago Argonne, LLC, under contract number DE-AC02-06CH11357. Work performed at the Center for Nanoscale Materials and Advanced Photon Source (17-BM, 11-ID-C and 32 ID-C) and both US Department of Energy (DOE), Office of Science User Facilities, was supported by the US DOE, Office of Basic Energy Sciences, under contract number DE-AC02-06CH11357. The use of NSLS-II (beamlines 3-ID, 7-BM and 18-ID) is supported by the US DOE, Office of Science User Facility, operated by the Brookhaven National Laboratory under contract number DE-SC0012704. Y.S.M. and J. Wang acknowledge support from the Energy Transition Network in the Institute for Climate and Sustainable Growth at the University of Chicago. Y.S.M. and J. Wang acknowledge startup funding from the Pritzker School of Molecular Engineering in the University of Chicago that supported J. Wang's full graduate fellowship.

Author contributions

J. Wang, T. Liu, Y.S.M. and K.A. conceived the idea and designed the experiments. J. Wang and T. Liu synthesized all the materials and conducted the electrochemical measurements. L.Y. and J. Wen carried out the SEM and TEM results. T. Liu, J. Wang, H.Z., W.X. and T. Li performed the ex situ/in situ synchrotron HEXRD and analysis. L.M., J. Wang, W.H. and H.Z. performed the ex situ XAS experiment and data analysis. X.H., M.V.H. and L.L. conducted the SDXM and data analysis. H.Z. performed the Brunauer–Emmett–Teller measurement and analysis. K.R. performed the FIB-EBSD experiment and analysis. X.X., W.H., J. Wang, T.Z. and R.A. performed the TXM and data analysis. J. Wang, T. Liu, Y.S.M. and K.A. wrote the paper and all authors edited the paper.

Competing interests

The authors declare no competing interests.

Additional information

Supplementary information The online version contains supplementary material available at https://doi.org/10.1038/s41565-025-02079-9.

Correspondence and requests for materials should be addressed to Tongchao Liu, Ying Shirley Meng or Khalil Amine.

Peer review information *Nature Nanotechnology* thanks Laura Simonelli, David Stephen Wragg and the other, anonymous, reviewer(s) for their contribution to the peer review of this work.